Unlocking Ultrastrong High-Temperature Ceramics via Non-Equimolar Refractory Metal High-Entropy Nitrides

Supplementary Material

O.V. Pshyk[a,b,c,d], A. Vasylenko[e], P. Küttel[f], B. Wicher[b,g], P. Schweizer[a], J. Michler[a], T.E.J. Edwards[a,h]

a Empa — Swiss Federal Laboratories for Materials Science and Technology, Laboratory for Mechanics of Materials and Nanostructures, Thun 3602, Switzerland

b Thin Film Physics Division, Department of Physics (IFM), Linkoping University, 581 83 Linkoping, Sweden

c NanoBioMedical Centre, Adam Mickiewicz University, Poznań, Poland

d Empa — Swiss Federal Laboratories for Materials Science and Technology, Laboratory for Surface Science and Coating Technology, Dübendorf 8600, Switzerland

e Department of Chemistry, University of Liverpool, Liverpool, United Kingdom

f Alemnis AG, Schorenstrasse 39, 3645 Gwatt, Switzerland

g Faculty of Materials Science and Engineering, Warsaw University of Technology, 02-507 Warsaw, Poland

h National Institute for Materials Science, Research Center for Structural Materials, 1-2-1 Sengen, Tsukuba, Ibaraki 305-0047, Japan

Supplementary Notes

Supplementary Note 1

Many studies on high-entropy ceramics focus on maximizing configurational entropy (using equimolar ratios of metal elements) for greater single-phase stabilization[12,13] of single-phase solid solution phase; differing combinations and increasing the number of elements has achieved properties often highly surpassing those of the constituent conventional ceramic components[13,14].

Although some ceramic systems demonstrate high-temperature stability[15,16], recent theoretical studies have shown that all 126 equimolar high-entropy nitrides studied in[17] are metastable with respect to all corresponding equimolar lower-entropy nitride phases that were confirmed experimentally and also proved in other works[16]. Therefore, we propose that exploiting the metastability of high-entropy ceramics can offer additional phase space, resulting in multiple advantages for tuning beneficial properties.

Supplementary Note 2

The local lattice disorder inherent in high-entropy ceramics arising from many different sized and chemically distinct elements and fluctuations in the local chemical environment influences the movement of diffusing species, defects, and dislocations[18,19]. Therefore, the high-entropy concept provides ample room for further well-targeted improvement of high-temperature mechanical properties[20]. While mechanical properties are enhanced by severe lattice distortion (solid-solution strengthening), nanograin microstructure impeding dislocation motion (Hall-Petch strengthening), and by changes in and/or elimination of lattice slip systems[21], the inhibition of grain coarsening typical for high-entropy ceramics at elevated temperatures allows to retain mechanical properties[16]. Theoretical calculations demonstrate that high-entropy ceramics show a slow reduction in tensile and shear strength with temperature[22]. Although only a few studies report the mechanical behavior of high-entropy ceramics at elevated temperatures[20,23,24], they demonstrate the exceptional potential of high-entropy ceramics to become new high-temperature materials[25]. However, most rare reports in the literature deal with *post-mortem* mechanical characterization of high-entropy ceramics, and their high-temperature mechanical properties under real operating conditions still lack detailed characterizations[19,26,27]. The possible reason for the latter is that most high-entropy ceramics are synthesized in thin film form. Owing to highly non-equilibrium conditions, physical vapor deposition (PVD) is typically the most preferential method for metastable high-entropy ceramic synthesis. Characterization of mechanical properties of thin films at high temperatures has not been feasible due to the limited volume available and related obstacles. However, recent advancements in thermomechanical testing methods for micro/nano-scale materials allow us to overcome the critical challenges associated with temperature control during material characterization, specimen size, and resolution of measurements[28].

Supplementary Note 3

In Fig. S10, the low elastic loading modulus measured at 800 or 900 °C, depending on composition, is arrowed; the lowest modulus is consistently associated with testing at 1000 °C. A measured relatively low modulus is despite the sensor drift corrections, temperature-dependent loading frame modulus correction, Fig. S15, and sink-in correction accounting for the minor (~10%) thermal reduction in elastic modulus of the (0001) sapphire substrate by 1000 °C were considered in prior. Initial suspicion of plastic deformation of the sapphire substrate at high temperature was proven incorrect: a cross-sectional lift out of a hexanary Al-high pillar compressed at 1000 °C imaged by TEM does not reveal either deviation of the film-substrate interface, nor evidence of remaining crystal defects in the sapphire (dislocations or twins), Fig. 4b. According to previous studies, fracture of sapphire at this temperature is preceded by deformation twinning[5]; hence as neither occurs here, this indicates that load applied to the micropillar is effectively distributed in the ~2 μm film thickness below the pillars.

To further elucidate this phenomenon, a TEM analysis of a central cross-section of the diamond punch itself was carried out. According to the SEM imaging, it is evident that imprints of the tops of the micropillars are left in the punch surface after testing up to 1000 °C, Fig. S11. Extensive chemical reactivity between punch and high-entropy refractory nitride pillars was observed, resulting in consumption of the punch and the formation of mechanically weaker oxide phases[29], as well as carbides, oxy-carbides and a carbo-nitride several hundred nanometres thick in total, Fig. S12. Specifically, we identify on the punch surface: AlO_x particles, (Zr, Hf)O_x particles, CN_x particles, a thin TiC_x layer, a thick (Ti, Zr, Hf, V, Nb, Ta, Al, Si)O_xC_y layer interfacing the diamond, and a SiO_x outer layer, where Si originates from a separate Si-doped refractory high-entropy nitride series.

In addition, evidence of mechanical deformation of the diamond (stacking faults on at least 4 distinct systems, as well as an elevated density of ordinary dislocations) was found after testing up to 1000 °C, Fig. S11; these faults are most dense near the contact interface between pillar and punch. Although this is not definitive proof of plasticity generated at high temperature – rather than initially present from punch production or related to low-temperature testing – it is consistent in both crystal deformation mechanism and applied stress (7.9 GPa, vs. ~8.5 GPa maximum here) with previous reports of plasticity in 3.5 GPa anvil-confined 5 μm diamond powder [30].

The chemical reactivity and mechanical deformation of the diamond punch are expected to have occurred most readily at the highest test temperatures, according to straightforward

kinetic arguments, and provide pathways for additional punch displacement to be achieved by a given load in the applied test conditions.

Supplementary Note 4

W-containing, heptanary nitride: TEM imaging and analysis following micro-compression at 1000 °C revealed extensive oxygen inward diffusion, Fig. S16, manifested as a high oxygen content along columnar grain boundaries in the upper third of the film, Fig. S17, and a ladder-like structure within the grains there, with the horizontal oxygen-rich rungs coincident with locally increased Hf and Zr atomic contents. Diffraction from the low volume of these additional phases was not captured in film's upper half's SAED. Grain-scale segregation of W remains, along with atom-scale segregation.

Supplementary Note 5

A simple, classic model of shear strength, τ_{sum}, based upon summative strengthening of contributors yields Eq. S.4, is composed as follows: solid solution strengthening of the metallic sub-lattice, τ_{SS}, supplements the temperature-dependent binary nitride lattice resistance, τ^*, Taylor hardening is given by τ_G, the effect of grain size, diameter d, on shear strength, $\tau_{h\text{-}p}$, supplements the source-strengthening, τ_S, stemming from the small sample size; finally the contribution of short-range ordering across the metallic sub-lattice is quantified by τ_{sr}, and spinodal decomposition yields the contribution τ_{sd}. Conversion to a uniaxial strength, σ, is achieved via the Taylor factor $M = 3.06$ for untextured face-centered cubic slipping on the close-packed planes.

$$\tau_{\mathrm{sum}} = \sigma/M = \tau^* + \tau_{\mathrm{SS}} + \tau_{\mathrm{G}} + \tau_{\mathrm{S}} + \tau_{\mathrm{h-p}} + \tau_{\mathrm{sr}} + \tau_{\mathrm{sd}} \quad \text{(S.4)}$$

$$\approx \left(1 - \frac{T}{T_c}\right)\left(\tau_0^* + \tau_{\mathrm{SS},0} + \tau_{\mathrm{sr},0}\right) + \alpha b G\sqrt{\rho} + KG\frac{\ln(\bar{\lambda}/b)}{\bar{\lambda}/b} + \frac{1}{M}K_{\mathrm{h-p}}d^{-1/2} + k_{\mathrm{s}}(A\eta Y)^{5/3}(\lambda/Gb)^{2/3} \quad \text{(S.4b)}$$

where material parameters are taken as those for the hexanary Al-high composition (lattice parameter: $a_{6\text{-Al-high}}$ = 4.2672 Å here), as measured and employed in calculations in[1]: shear modulus, G = 168 GPa, the ½<110> Burgers vector of slip, b = 3.017 Å, the modulus term $Y = E(1-\nu)$, with Young's modulus E = 453 GPa and Poisson ratio ν = 0.209; $k_s = 0.122[\pi(1-\nu)(1-2\nu)]^{2/3}$ is another material elasticity term. Further parameters include the dislocation density, ρ, taken as 10^{15} m^{-2} here, $K_{h\text{-}p}$ = 12.5 GPa nm$^{-1/2}$ the Hall-Petch constant (taken for TiN[31]), a d = 100 nm grain size, micropillar diameter D = 1800 nm which

approximates the average source length $\bar{\lambda}$, and pre-factors $K = 0.5$ & $\alpha = 0.1$. The solid solution- and short-range order-strengthened lattice resistance prefactor is approximated here as: $\left(\tau_0^* + \tau_{\mathrm{SS},0} + \tau_{\mathrm{sr},0}\right) = 4.5$ GPa; T_c is a critical temperature (beyond the temperature range probed here), above which lattice resistance is assumed constant and low. With regards to the spinodal itself, $A = (C - C_0) / 3$, is the amplitude of each of the three dimensional composition modulation components on the metallic sub-lattice, giving $A = (92 - 51) / 3 = 13.7$ at.% here for the Al composition in the hexanary Al-high nitride after annealing at 1200 °C, Fig. 2f, whilst $\eta = a^{-1}\, da/dC$ is the relative lattice parameter change against composition, and the spinodal wavelength of a specific material and annealing condition is λ. Upon further inspection the equation for the spinodal component simplifies if Vegard's law of proportionality between isostructural solid solutions' compositions and their lattice parameters holds true: hence $\eta \approx a^{-1}\, \Delta a/\Delta C$ where Δ denotes a finite change in a value, with the result that $A\eta$, and thereby τ_{sd}, can be expressed as a function of the amplitude of the change in lattice parameter across the spinodal, without including the explicit value of composition change itself – which cancels between A and η. It is evident that any real deviations from Vegard's law leading to an increased da/dC will yield additional strengthening. The lattice parameter of cubic AlN is taken as 4.045 Å.

Supplementary Tables

Supplementary Table 1. Elemental composition of the samples derived from the combined measurements using XPS and ToF-ERDA.

Sample	Composition (at.%)											
	N	**Al**	**Ti**	**Hf**	**V**	**Zr**	**Nb**	**Ta**	**W**	**Ar**	**O**	**C**
(TiVZrNbHf)N	48.2	–	11.8	7.6	10.5	12.2	7.8	–	–	0.4	0.8	0.7
$(TiVZrNbHf)_{0.86}Al_{0.14}N$	48	6.9	10.3	6.5	9.0	10.2	6.8	–	–	0.4	1	0.8
$(TiVZrNbHf)_{0.49}Al_{0.51}N$	48.8	25.0	6.3	3.4	5.1	5.8	3.5	–	–	0.4	0.8	0.7
(TiVZrNbHfTa)N	48.2	–	11.5	7.6	6.9	10.4	6.5	6.7	–	0.5	0.9	0.8
(TiVZrNbHfTaW)N	45.0	–	9.7	5.6	7.3	9.5	5.9	5.6	9.6	0.5	0.6	0.9

Supplementary Table 2. Reduced Young's moduli derived from nanoindentation measurements for all films performed before and after annealing in a vacuum at different temperatures of 900-1200 °C .

Nominal composition	RT	900 °C	1000 °C	1100 °C	1200 °C
(TiVZrNbHf)N	353.9±9.3	375.9±12.2	385.3±9.9	360.4±12.1	387.2±5.7
$(TiVZrNbHf)_{0.86}Al_{0.14}N$	365.9±9.8	382.6±10.6	384.8±9.3	387.5±14.9	383.7±10.8
$(TiVZrNbHf)_{0.49}Al_{0.51}N$	349.4±7.1	371.5±8.2	386.5±9.5	371.9±7.8	376.7±6.2
(TiVZrNbHfTa)N	370.6±12.4	383.17±11.4	380.8±9.6	381.9±13.3	382.8±11.1
(TiVZrNbHfTaW)N	390.4±8.7	393.2±9.4	369.0±9.4	403.3±5.9	364.6±11.1

Supplementary Figures

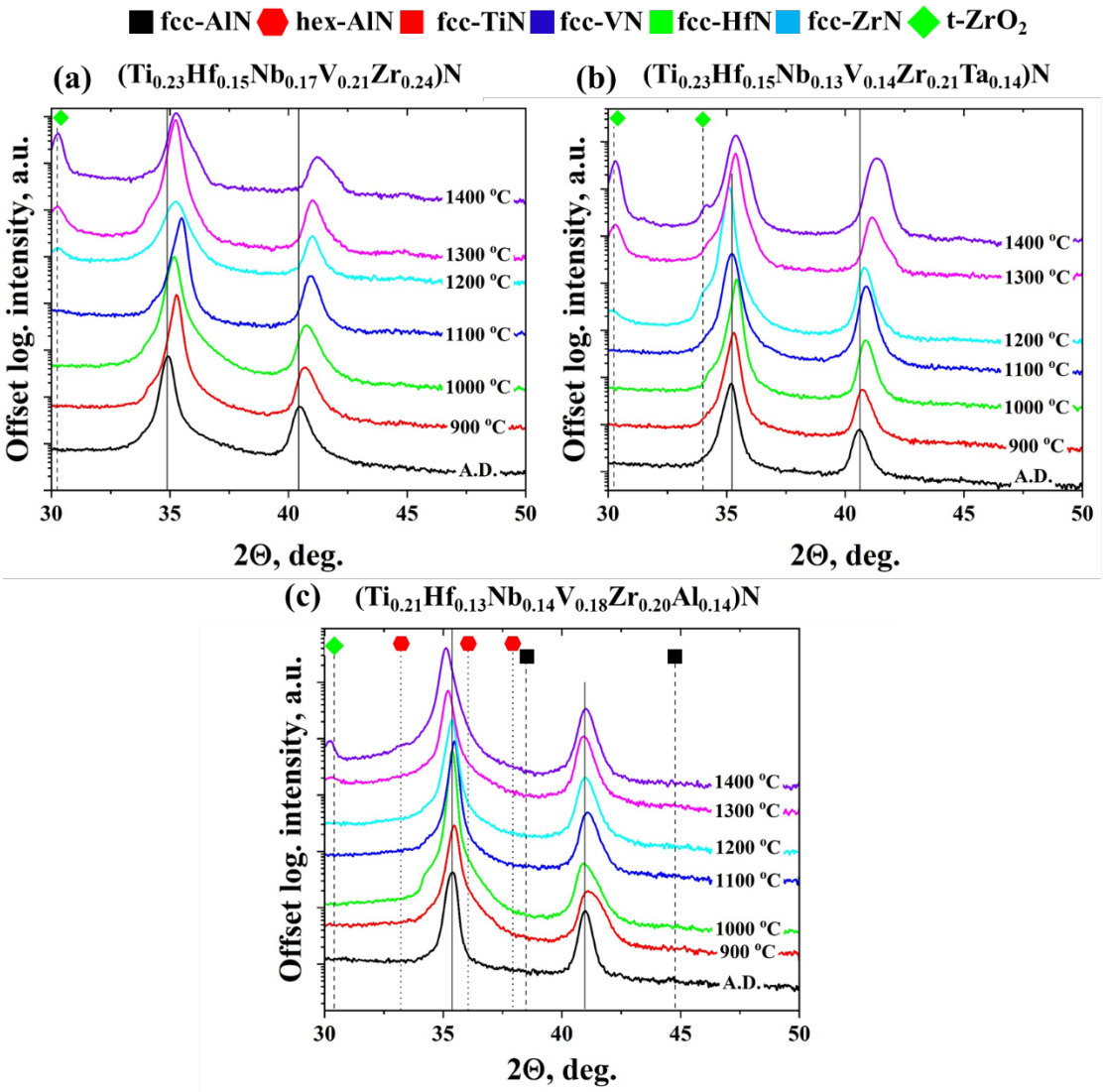

Supplementary Fig. 1. (a-c) XRD patterns for pentanary $(Ti_{0.23}Hf_{0.15}Nb_{0.17}V_{0.21}Zr_{0.24})N$, hexanary $(Ti_{0.23}Hf_{0.15}Nb_{0.13}V_{0.14}Zr_{0.21}Ta_{0.14})N$, and hexanary 'Al-low' $(Ti_{0.21}Hf_{0.13}Nb_{0.14}V_{0.18}Zr_{0.20}Al_{0.14})N$ thin films before and after annealing in vacuum at 900, 1000, 1100, and 1200 °C.

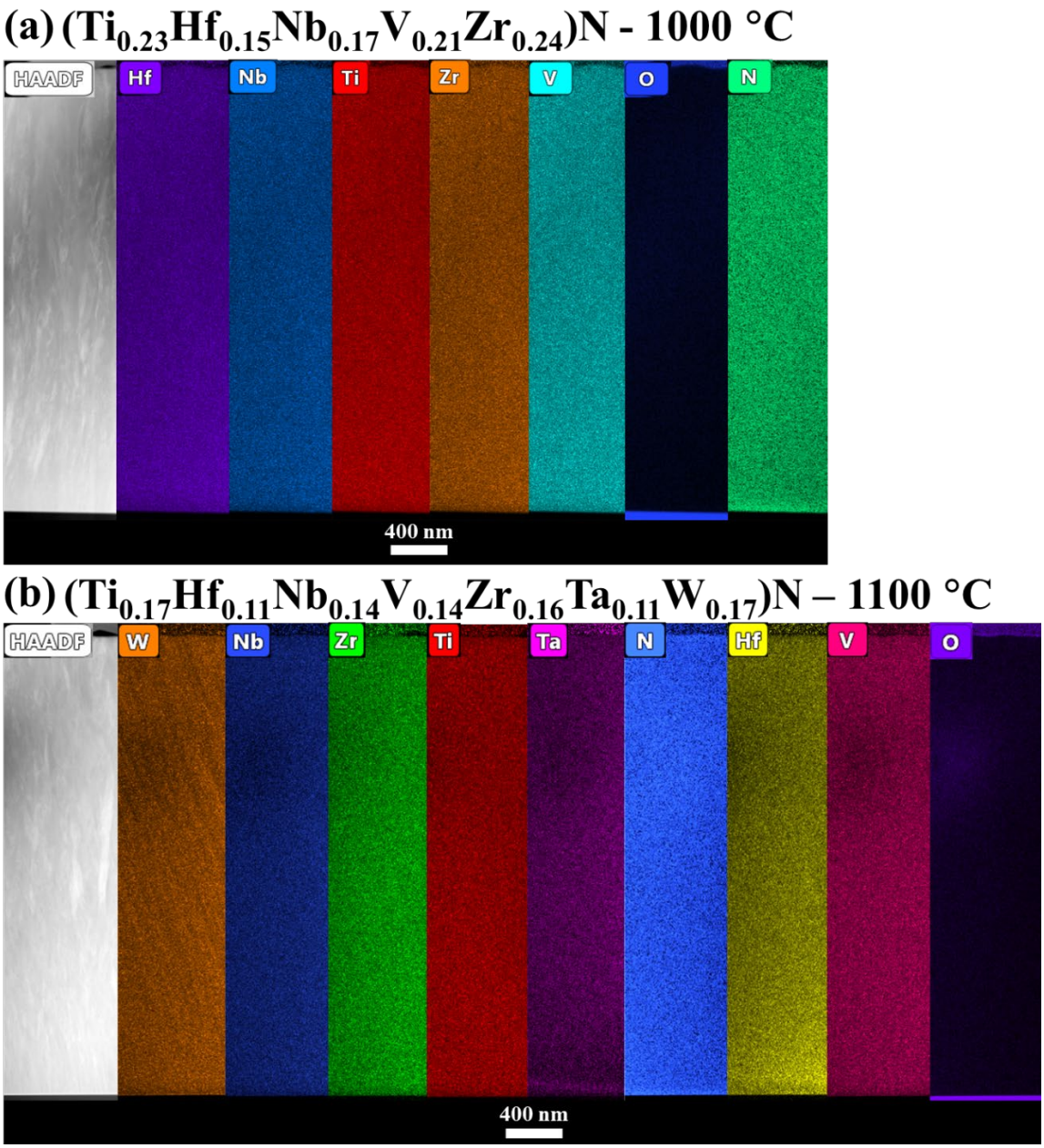

Supplementary Fig. 2. EDX color-coded elemental maps acquired from (a) pentanary nitride annealed at 1000 °C and (b) heptanary nitride annealed at 1100 °C.

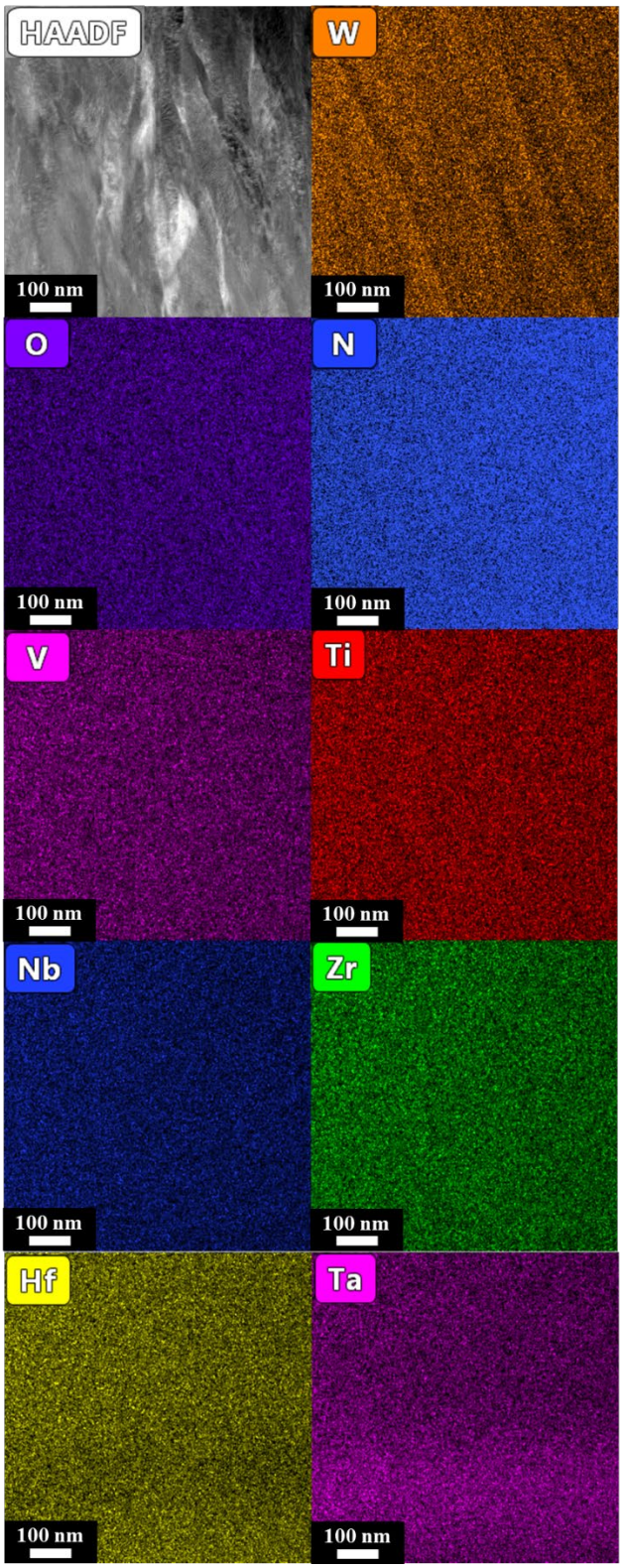

Supplementary Fig. 3 Magnified EDX color-coded elemental maps acquired from heptanary nitride annealed at 1100 °C.

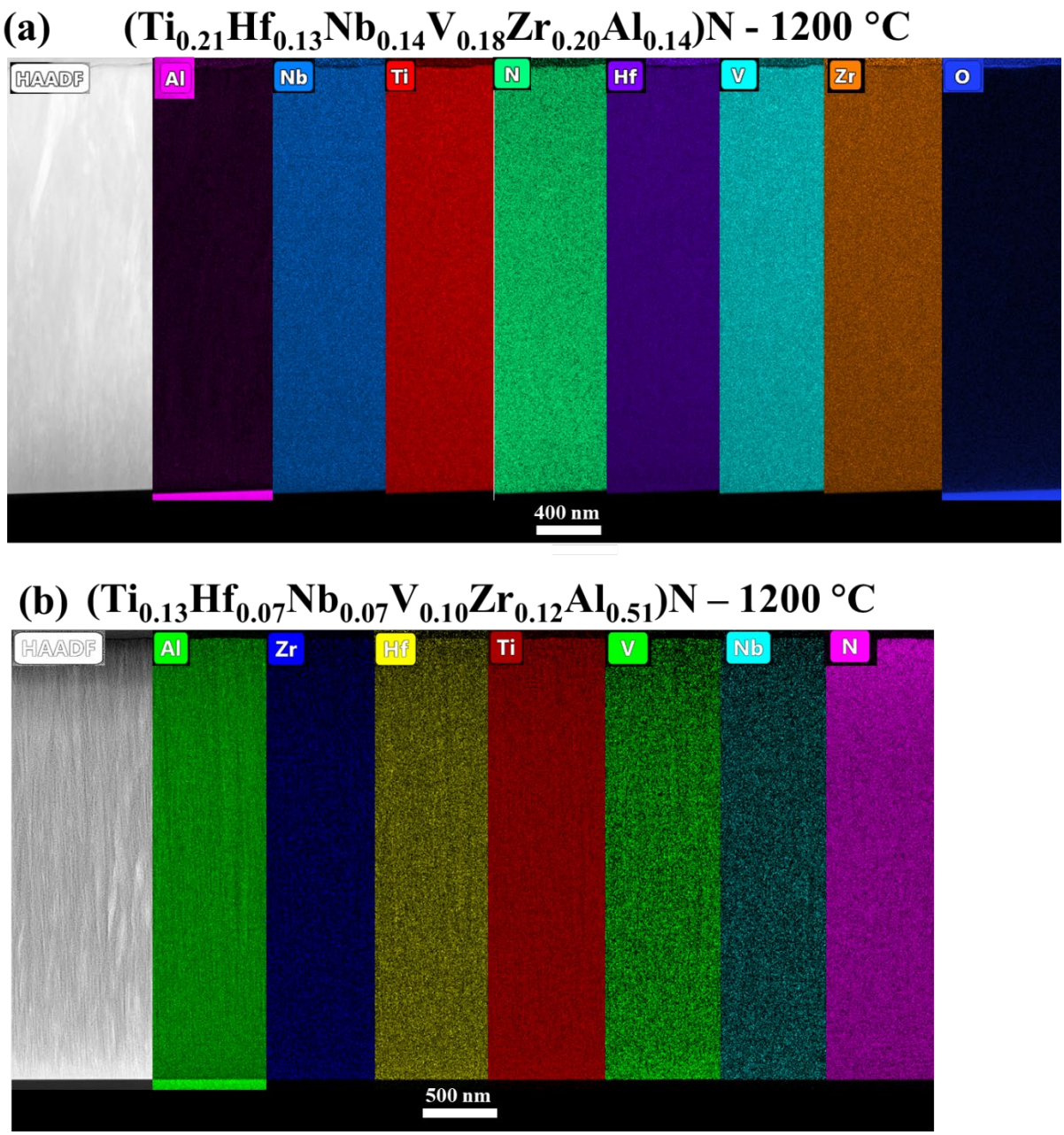

Supplementary Fig. 4. EDX color-coded elemental maps acquired from (a) the hexanary 'Al-low' $(Ti_{0.21}Hf_{0.13}Nb_{0.14}V_{0.18}Zr_{0.20}Al_{0.14})N$ and (b) hexanary 'Al-high' $(Ti_{0.13}Hf_{0.07}Nb_{0.07}V_{0.10}Zr_{0.12}Al_{0.51})N$ films after annealing at 1200 °C.

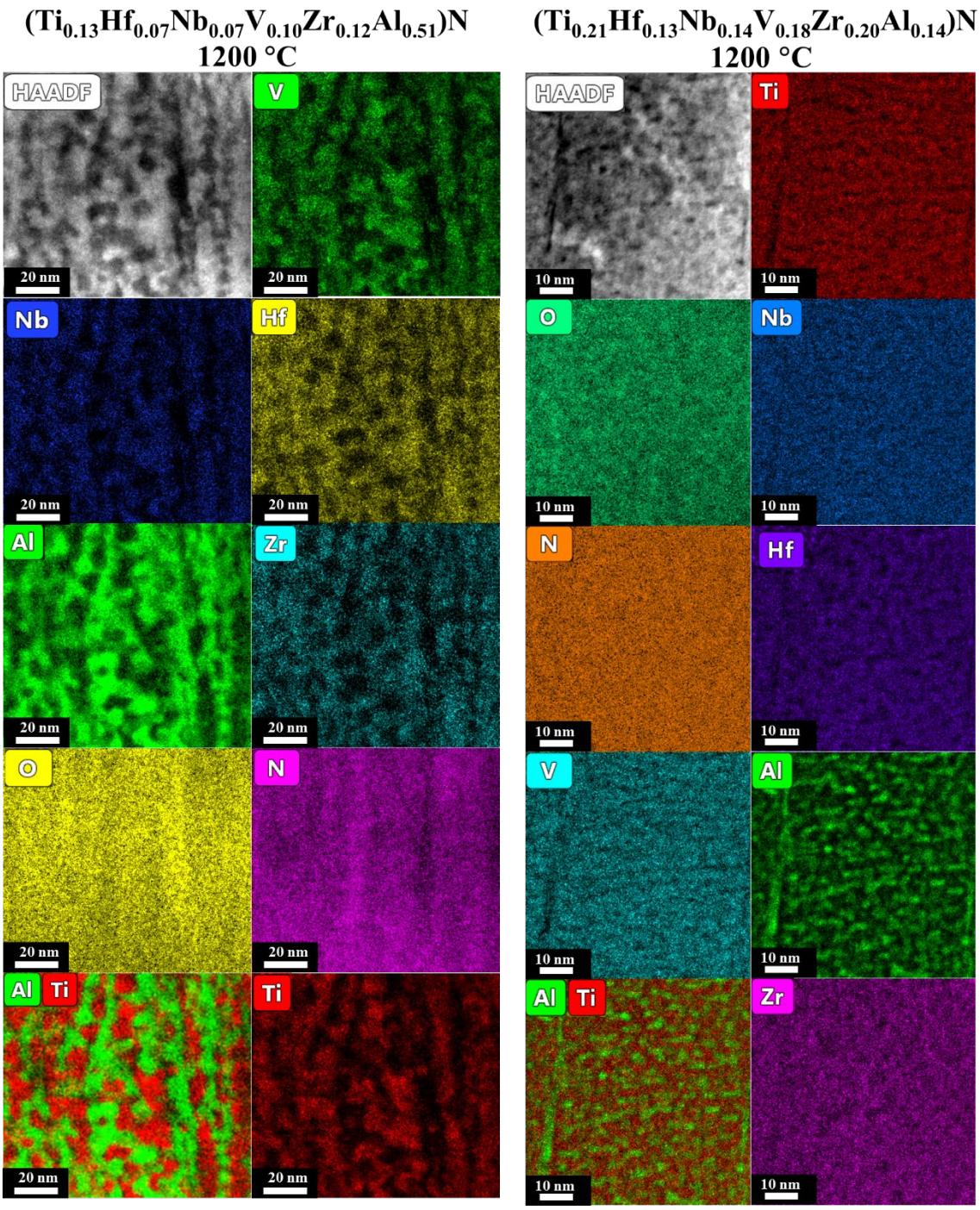

Supplementary Fig. 5 Magnified EDX color-coded elemental maps acquired from the hexanary 'Al-high' $(Ti_{0.13}Hf_{0.07}Nb_{0.07}V_{0.10}Zr_{0.12}Al_{0.51})N$ and the hexanary 'Al-low' $(Ti_{0.21}Hf_{0.13}Nb_{0.14}V_{0.18}Zr_{0.20}Al_{0.14})N$ films after annealing at 1200 °C.

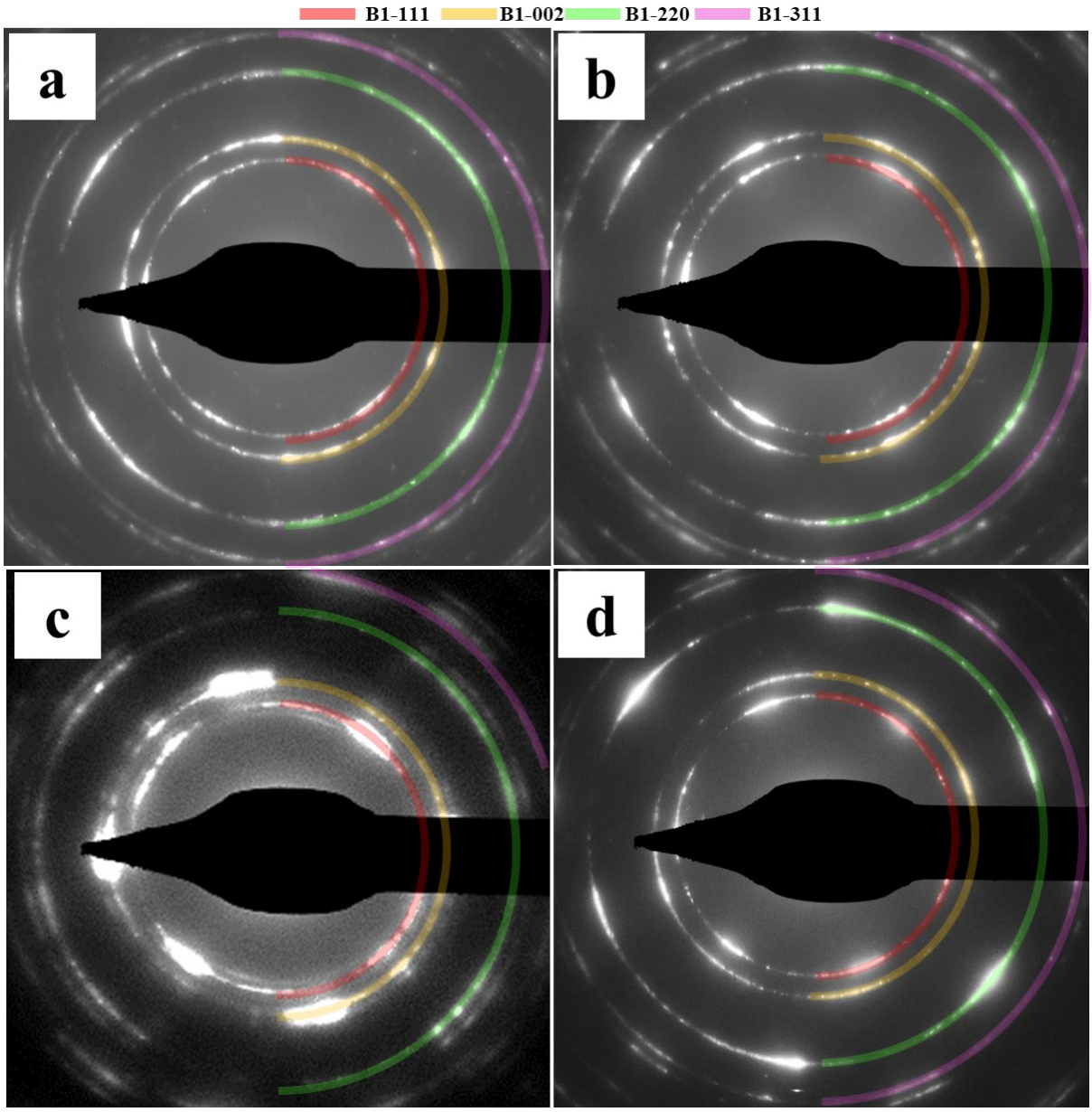

Supplementary Fig. 6. SAED acquired from (a) heptanary nitride annealed at 1100 °C, (b) pentanary nitride annealed at 1000 °C, (c) hexanary 'Al-high' and (d) hexanary 'Al-low' films after annealing at 1200 °C. The film growth direction is horizontal for the SAEDs presented here.

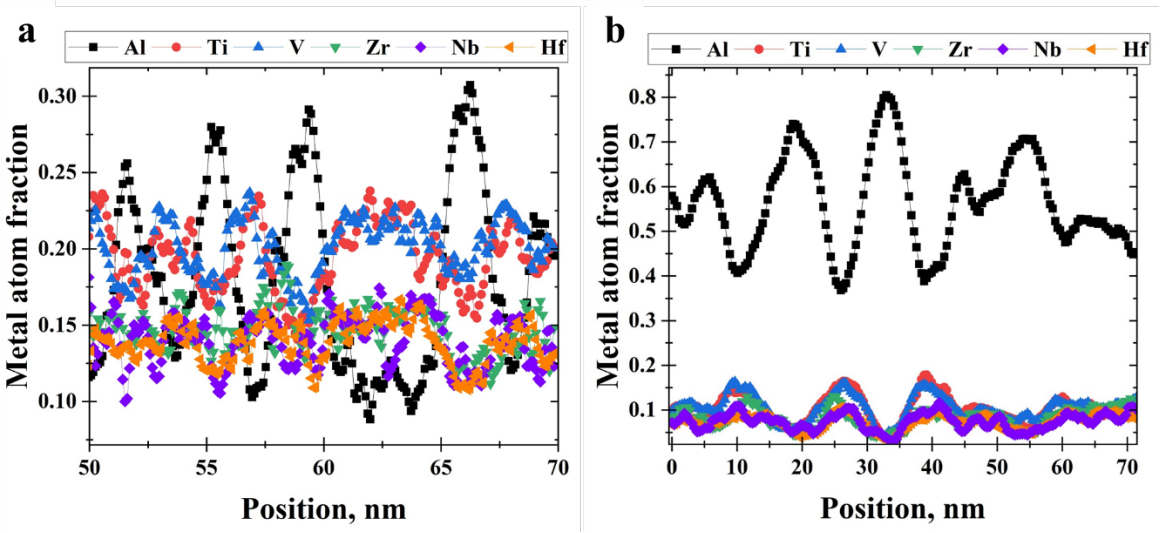

Supplementary Fig. 7. EDS line scans acquired from (a) hexanary 'Al-low' and (b) hexanary 'Al-high' films after annealing at 1200 °C.

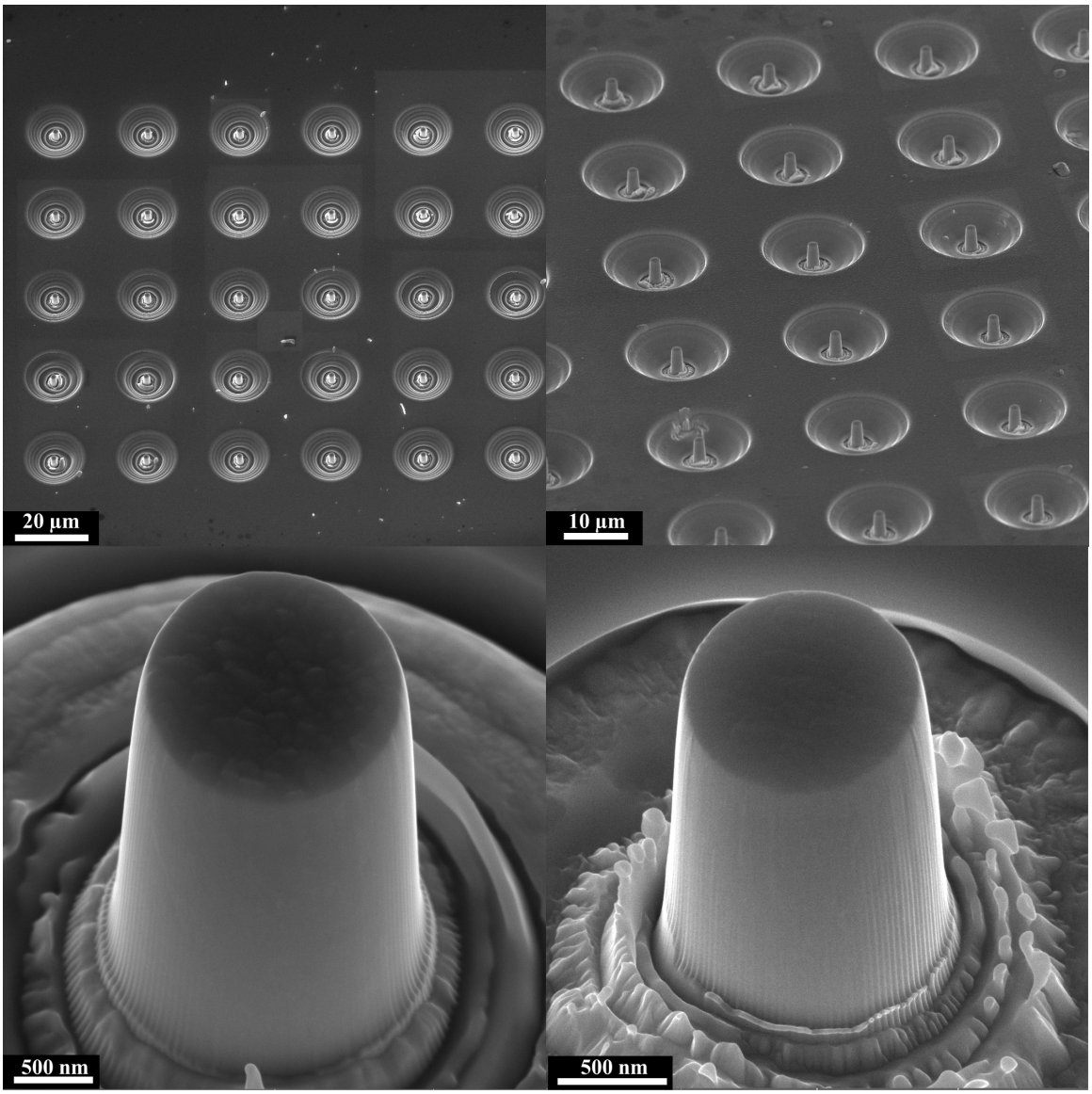

Supplementary Fig. 8. SEM images of representative sets of FIB-milled micro-pillars before microcompression, viewed at several tilt angles.

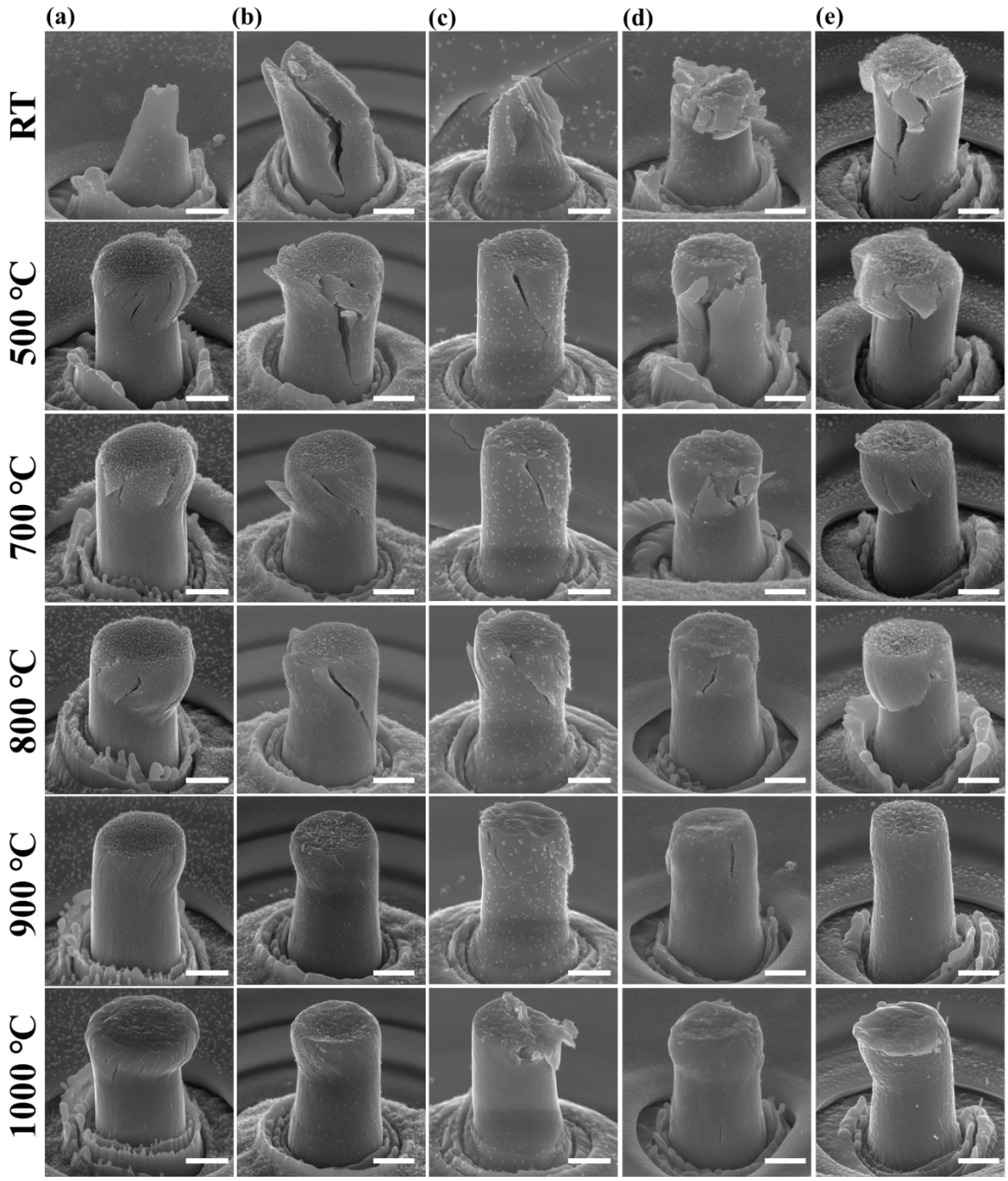

Supplementary Fig. 9. SEM images of micro-pillars deformation and fracture for (a) pentanary, (b) hexanary, (c) heptanary, (d) hexanary Al-low and (e) Al-high systems after compression at room temperature (RT), 500 °C, 700 °C, 800 °C, 900 °C, and 1000 °C. All scale bars are 1 μm.

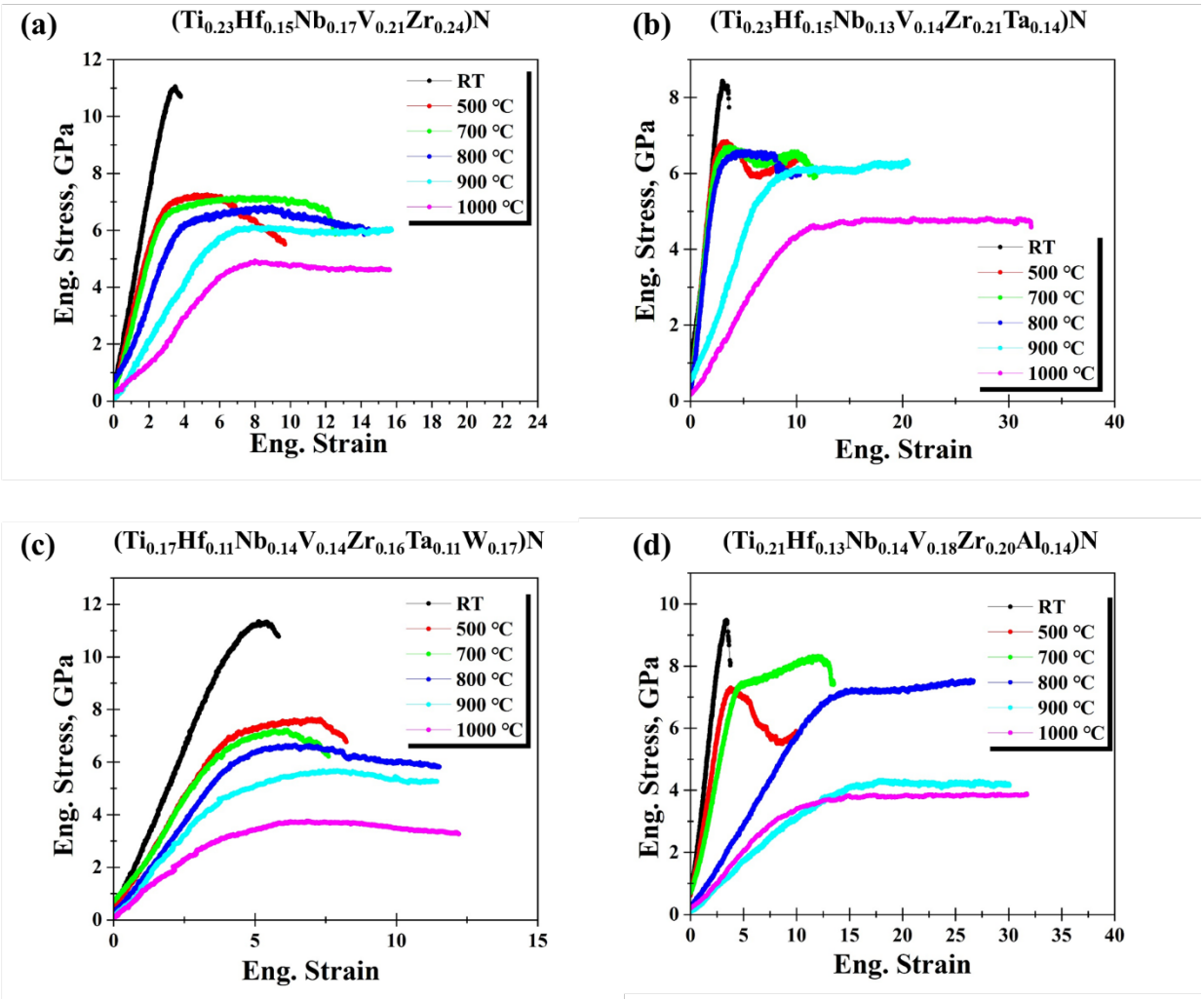

Supplementary Fig. 10. A set of stress-strain curves for (a) pentanary $(Ti_{0.23}Hf_{0.15}Nb_{0.17}V_{0.21}Zr_{0.24})N$, (b) hexanary $(Ti_{0.23}Hf_{0.15}Nb_{0.13}V_{0.14}Zr_{0.21}Ta_{0.14})N$, and (c) heptanary $(Ti_{0.17}Hf_{0.11}Nb_{0.14}V_{0.14}Zr_{0.16}Ta_{0.11}W_{0.17})N$, (d) the hexanary Al-low $(Ti_{0.21}Hf_{0.13}Nb_{0.14}V_{0.18}Zr_{0.20}Al_{0.14})N$ systems compressed at RT, 500 °C, 700 °C, 800 °C, 900 °C, and 1000 °C. For statistical accuracy, at least 4-5 pillars are compressed for each film composition at each test temperature, but only representative stress-strain curves are shown here.

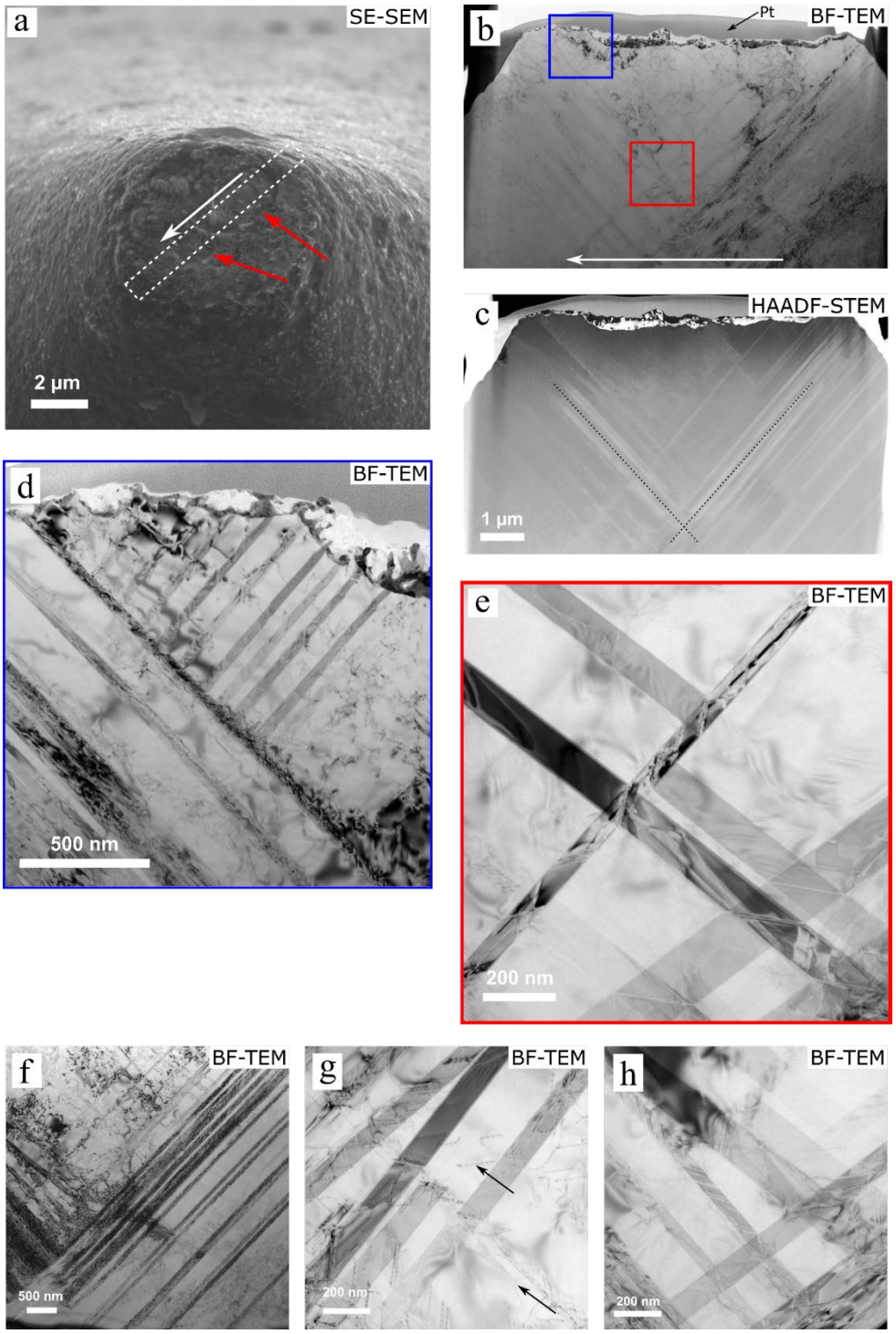

Supplementary Fig. 11. (a) SEM image of the diamond punch after compression up to 1000 °C with pillar imprints arrowed in red and cross-section lift-out location indicated; (b, c) BF-TEM and STEM-HAADF overview images of the punch cross-section, oriented by the white arrows in (a, b), with significant intersecting slip traces indicated (dotted black lines in (c)). BF-TEM images of the crystal deformation structures (d) in the region near the micropillar contact surface, indicated in (b) and (e - h) at the intersection of significant stacking fault families, where the stacking fault density is high. Black arrows in (g) indicate ordinary dislocations.

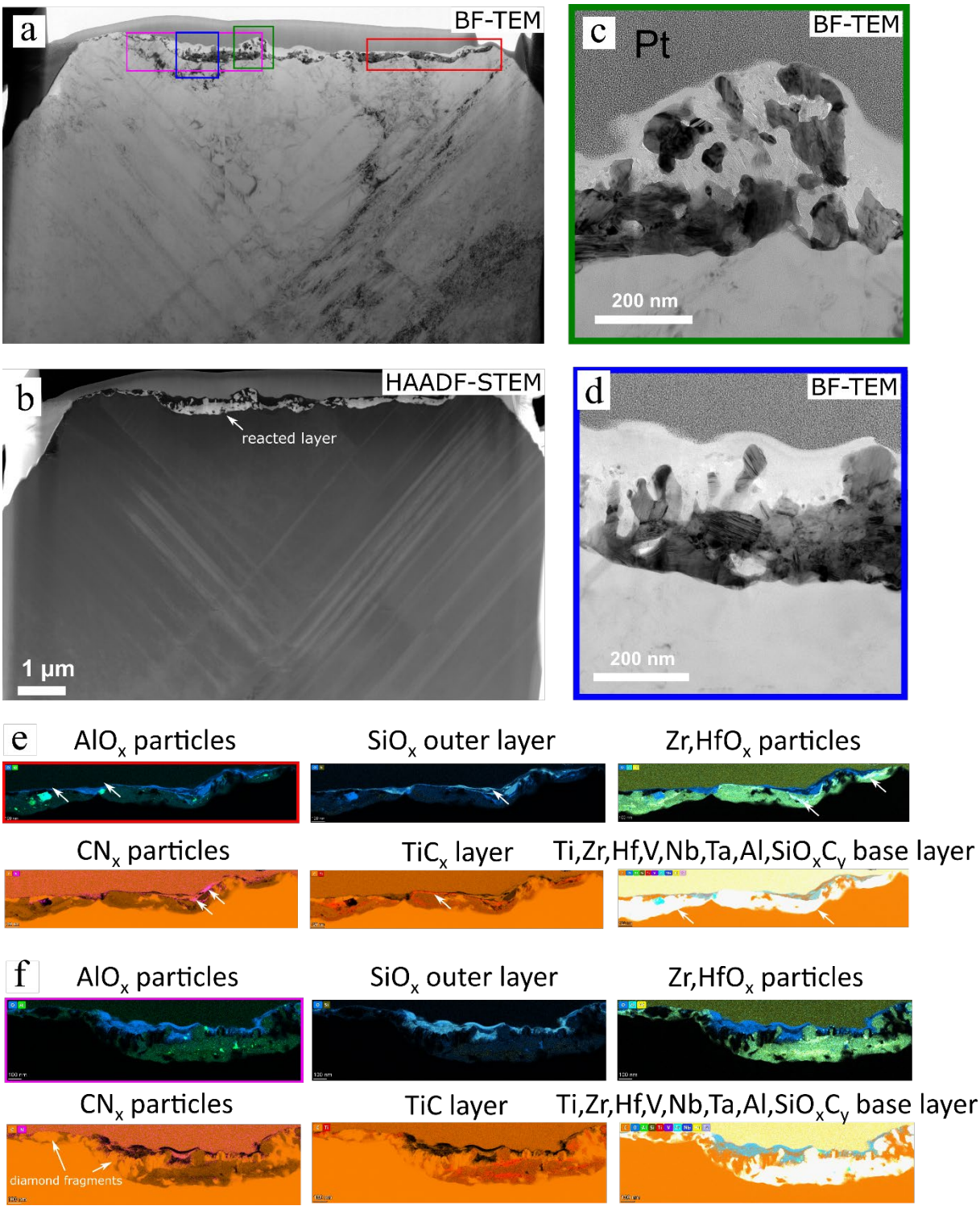

Supplementary Fig. 12. (a, b) BF-TEM and STEM-HAADF overview images of the punch cross-section, (c, d) High magnification BF-TEM images of the reacted layer, and (e, f) STEM-EDX analysis of the reaction products, indicated by white arrows in each case, observed in the cross-section of the diamond punch after compression up to 1000 °C, taken from the regions highlighted in (a).

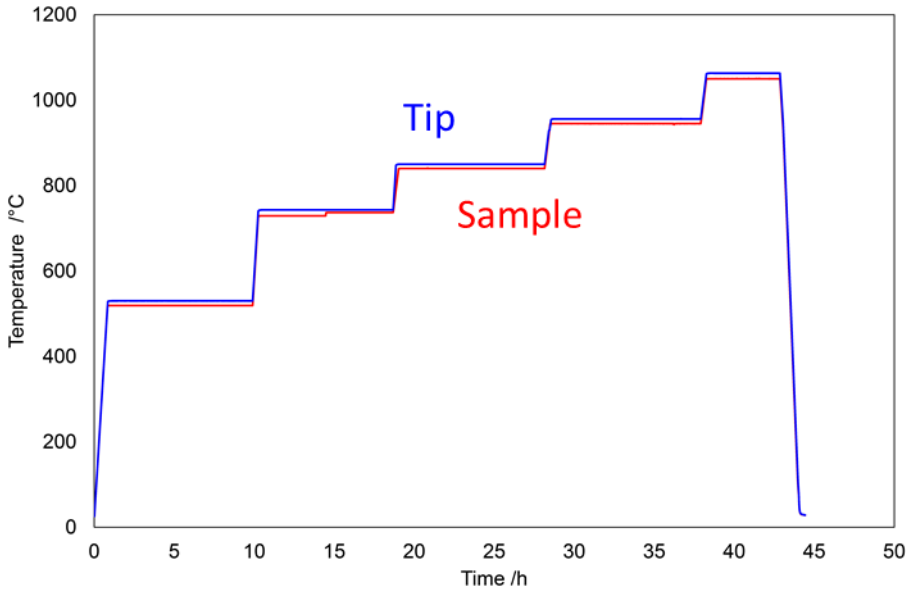

Supplementary Fig. 13. Temperature profile of a representative high-temperature microcompression experiment: measured temperatures of tip and sample side thermocouples.

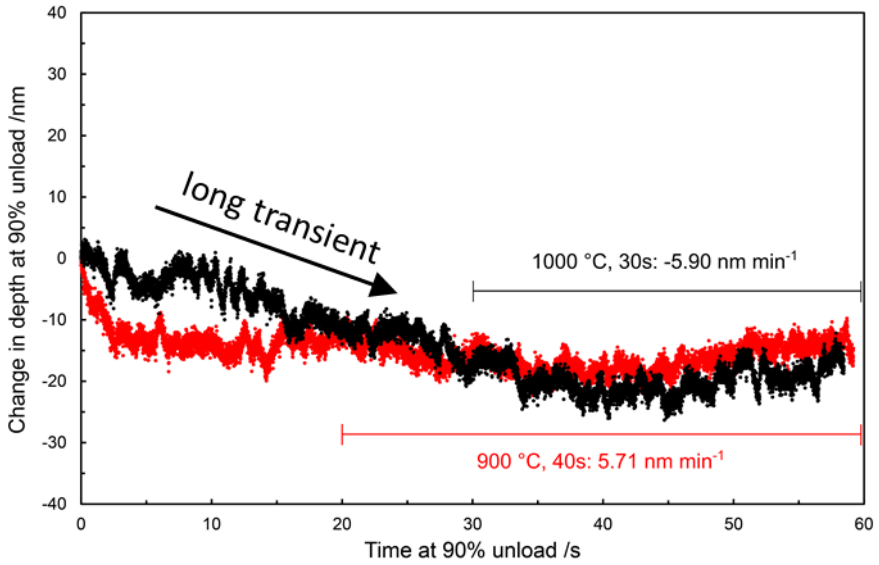

Supplementary Fig. 14. Displacement drift curves at constant load (upon 90% unloading) for temperature matching at 900 and 1000 °C.

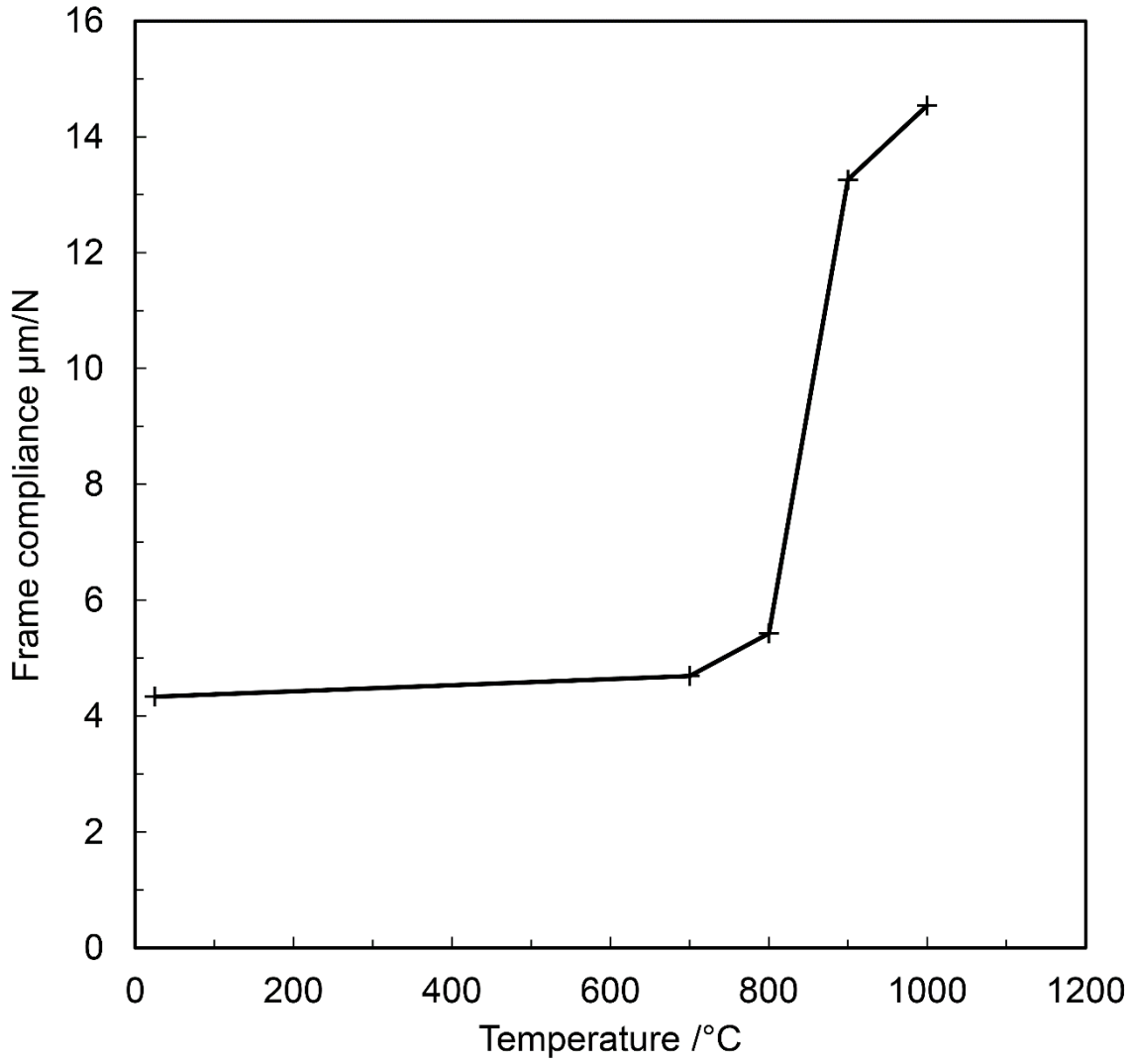

Supplementary Fig. 15. Rig compliance of the high-temperature nanoindentation setup against test temperature measured using a conductive diamond Berkovich on (0001) sapphire.

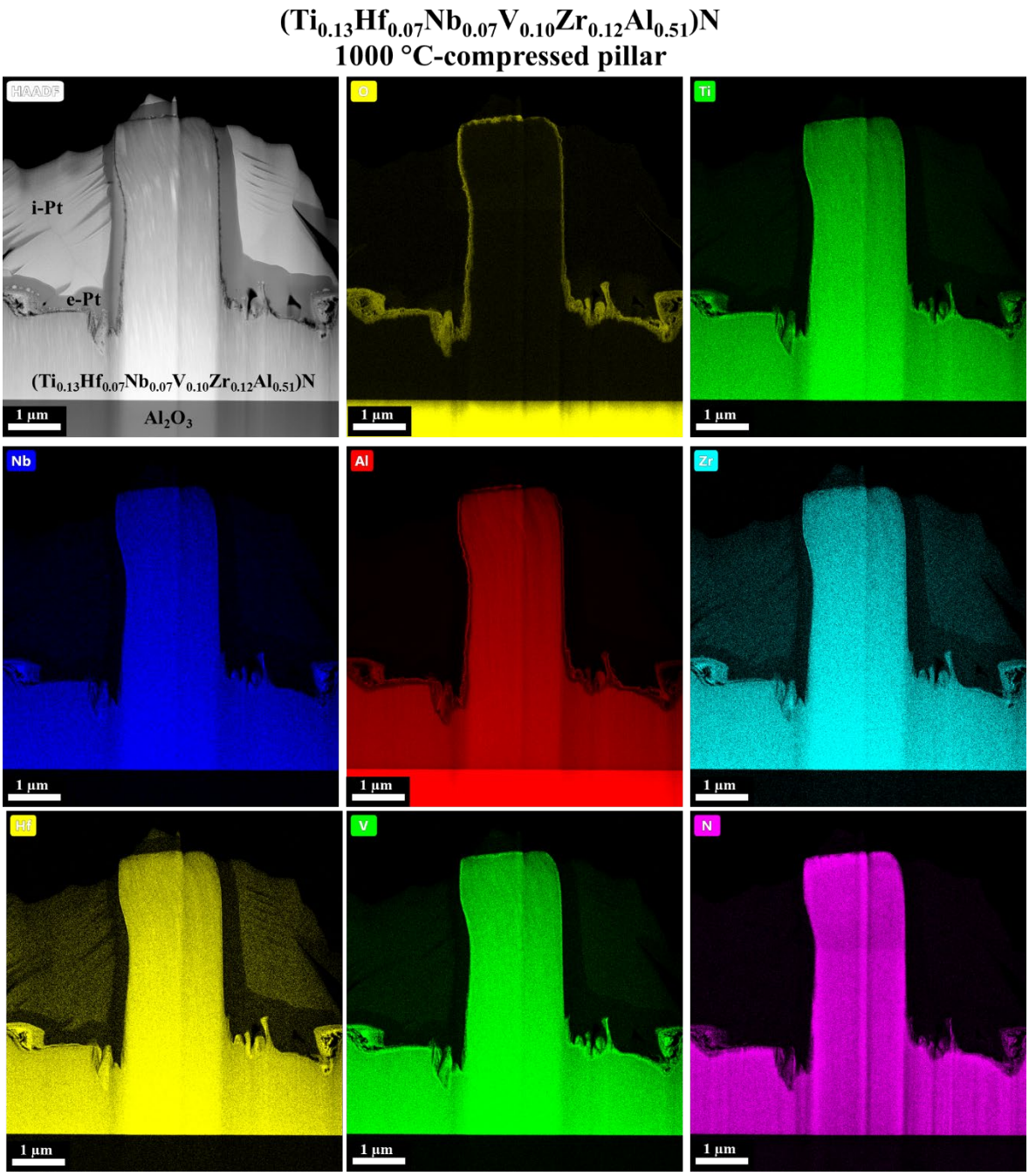

Supplementary Fig. 16. STEM-EDX color-coded elemental maps acquired from the hexanary Al-high pillar after compression at 1000 °C.

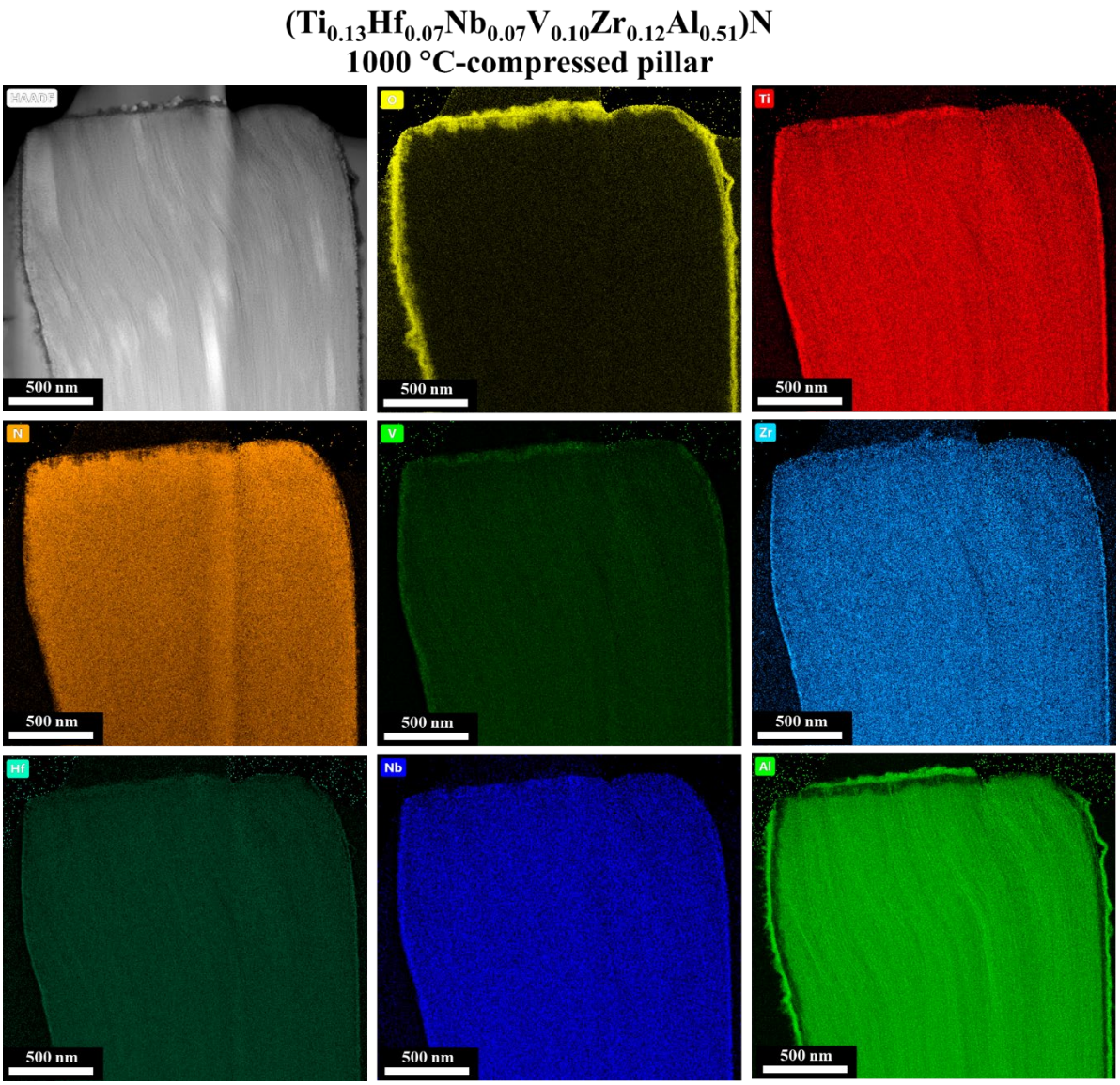

Supplementary Fig. 17. STEM-EDX color-coded elemental maps acquired from the upper part of the hexanary Al-high pillar after compression at 1000 ℃.

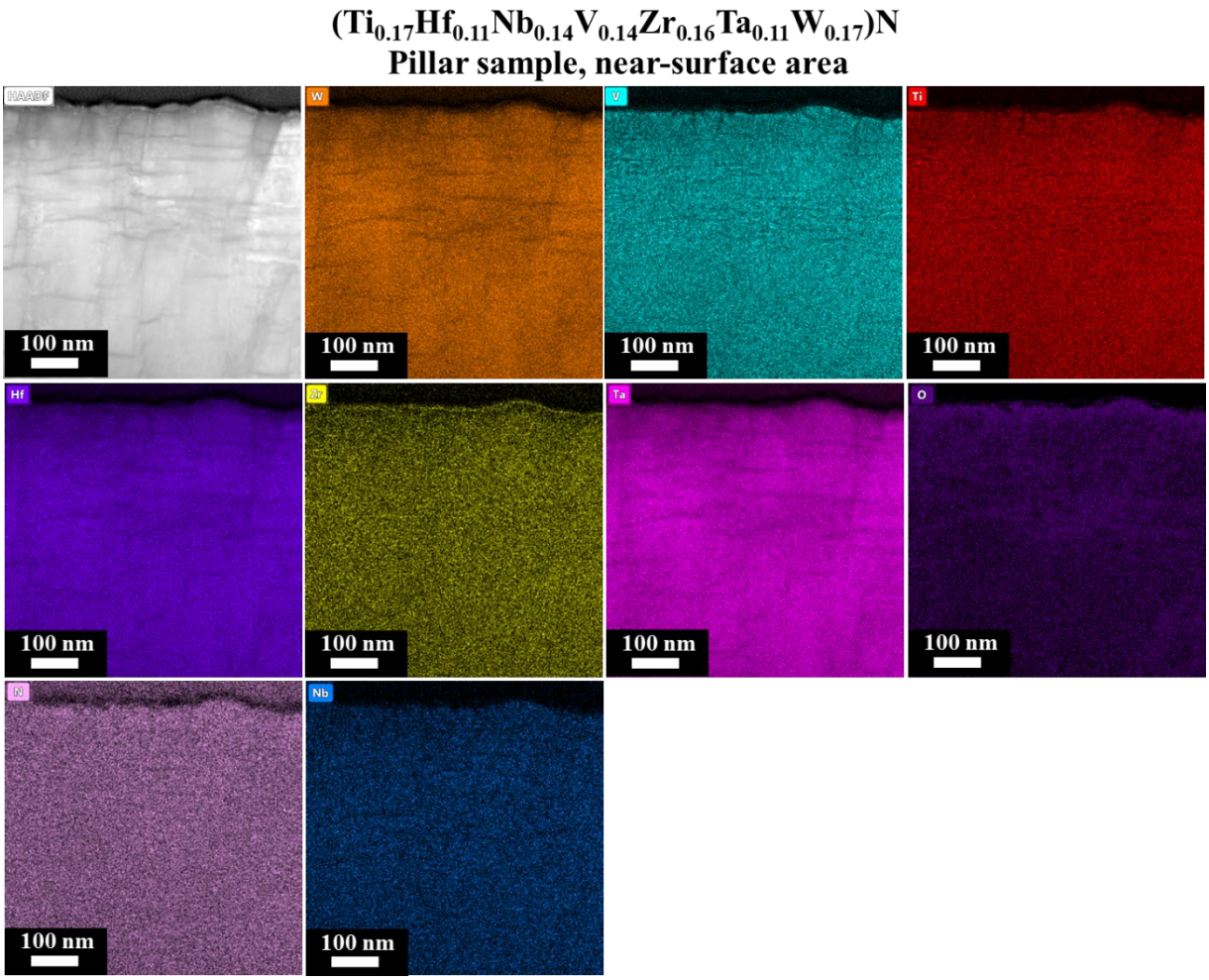

Supplementary Fig. 18. Magnified STEM-EDX color-coded elemental maps acquired from the near-surface area of the heptanary nitride film after micropillar compression tests at 1000 °C.

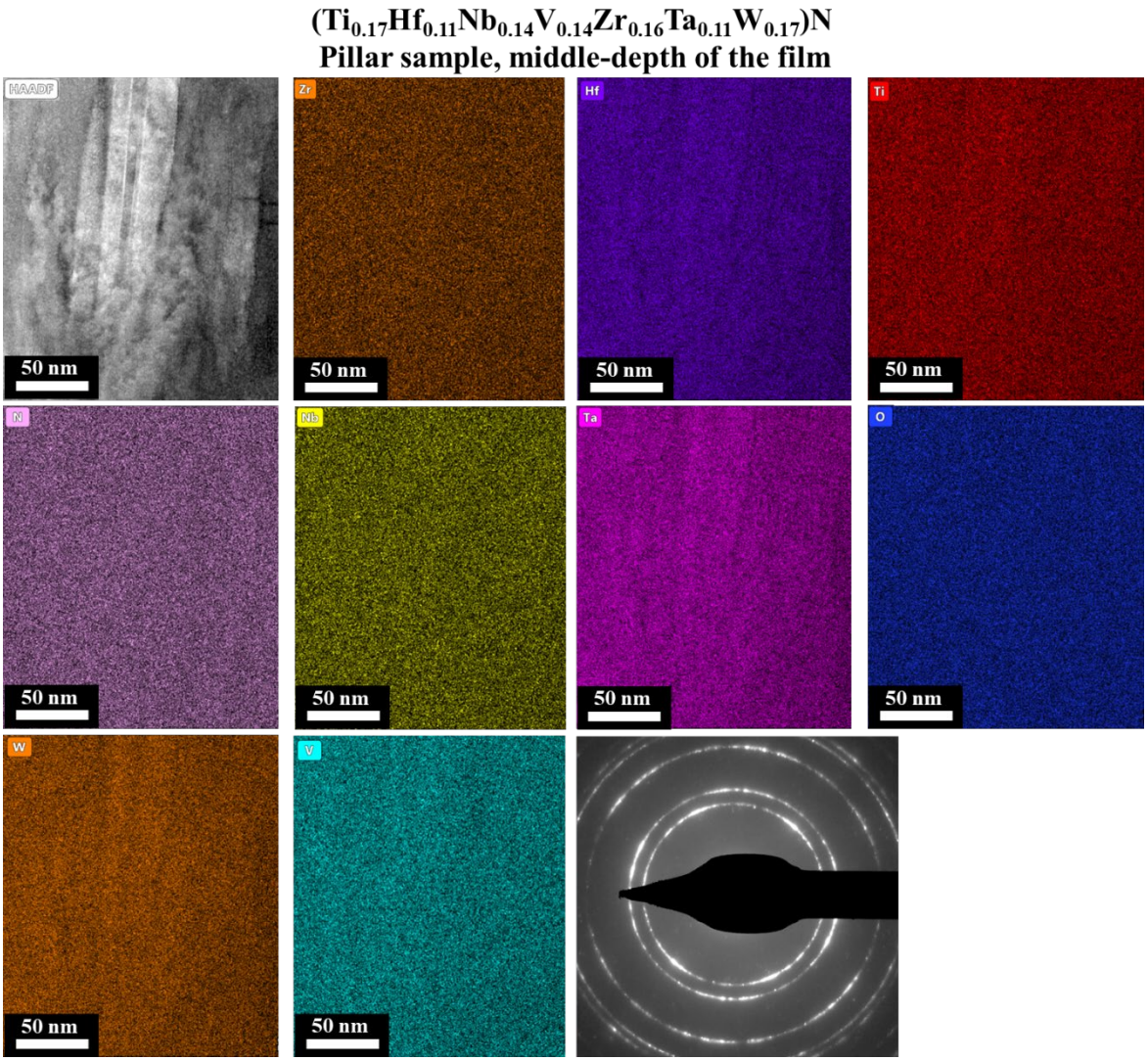

Supplementary Fig. 19. Magnified STEM-EDX color-coded elemental maps acquired from the mid-depth of the heptanary nitride film after micropillar compression tests at 1000 °C and corresponding SAED.

Additional References

1. Pshyk, A. V. *et al.* High-entropy transition metal nitride thin films alloyed with Al: Microstructure, phase composition and mechanical properties. *Mater. Des.* **219**, 110798 (2022).
2. Wheeler, J. M. & Michler, J. Elevated temperature, nano-mechanical testing in situ in the scanning electron microscope. *Rev. Sci. Instrum.* **84**, (2013).
3. Edwards, T. E. J. *et al.* Longitudinal twinning in a TiAl alloy at high temperature by in situ microcompression. *Acta Mater.* **148**, 202–215 (2018).
4. Oliver, W. C. C. & Pharr, G. M. M. Improved technique for determining hardness and elastic modulus using load and displacement sensing indentation experiments. *J. Mater. Res.* **7**, 1564–1580 (1992).
5. Schmid, F. & Harris, D. C. Effects of crystal orientation and temperature on the strength of sapphire. *J. Am. Ceram. Soc.* **81**, 885–893 (1998).
6. Wachtman, J. B. & Lam, D. G. Young's Modulus of Various Refractory Materials as a Function of Temperature. *J. Am. Ceram. Soc.* **42**, 254–260 (1959).
7. Zhang, H., Schuster, B. E., Wei, Q. & Ramesh, K. T. The design of accurate micro-compression experiments. *Scr. Mater.* **54**, 181–186 (2006).
8. van de Walle, A. Multicomponent multisublattice alloys, nonconfigurational entropy and other additions to the Alloy Theoretic Automated Toolkit. *Calphad Comput. Coupling Phase Diagrams Thermochem.* **33**, 266–278 (2009).
9. Jain, A. *et al.* Commentary: The materials project: A materials genome approach to accelerating materials innovation. *APL Mater.* **1**, (2013).
10. Kresse, G. & Hafner, J. Ab initio molecular dynamics for liquid metals. *Phys. Rev. B* **47**, 558–561 (1993).
11. Kresse, G. & Hafner, J. Ab initio molecular-dynamics simulation of the liquid-metalamorphous- semiconductor transition in germanium. *Phys. Rev. B* **49**, 14251–14269 (1994).
12. Li, W., Liu, P. & Liaw, P. K. Microstructures and properties of high-entropy alloy films and coatings: A review. *Mater. Res. Lett.* **6**, 199–229 (2018).
13. Oses, C. High-entropy ceramics. *Nat. Rev. Mater.* **5**, 295–309 (2020).
14. Akrami, S., Edalati, P., Fuji, M. & Edalati, K. High-entropy ceramics : Review of principles , production and applications. *Mater. Sci. Eng. R* **146**, 100644 (2021).
15. Chang, H.-W. *et al.* Influence of substrate bias, deposition temperature and post-deposition annealing on the structure and properties of multi-principal-component (AlCrMoSiTi)N coatings. *Surf. Coatings Technol.* **202**, 3360–3366 (2008).
16. Huang, P. & Yeh, J. Inhibition of grain coarsening up to 1000 ° C in (AlCrNbSiTiV) N superhard coatings. *Scr. Mater.* **62**, 105–108 (2010).
17. Kretschmer, A. *et al.* Strain-stabilized Al-containing high-entropy sublattice nitrides. *Acta Mater.* **224**, 117483 (2022).

18. Pickering, E. J. & Jones, N. G. High-entropy alloys: a critical assessment of their founding principles and future prospects. *Int. Mater. Rev.* **61**, 183–202 (2016).

19. Kirnbauer, A. *et al.* Mechanical properties and thermal stability of reactively sputtered multi- principal-metal Hf-Ta-Ti-V-Zr nitrides. *Surf. Coat. Technol.* **389**, 125674 (2020).

20. Feng, L., Chen, W. T., Fahrenholtz, W. G. & Hilmas, G. E. Strength of single-phase high-entropy carbide ceramics up to 2300°C. *J. Am. Ceram. Soc.* **104**, 419–427 (2021).

21. Castle, E., Csanádi, T., Grasso, S., Dusza, J. & Reece, M. Processing and Properties of High- Entropy Ultra-High Temperature Carbides. *Sci. Rep.* **8**, 1–12 (2018).

22. Sangiovanni, D. G., Mellor, W., Harrington, T., Kaufmann, K. & Vecchio, K. Enhancing plasticity in high-entropy refractory ceramics via tailoring valence electron concentration. *Mater. Des.* **209**, 109932 (2021).

23. Demirskyi, D. *et al.* High-temperature flexural strength performance of ternary high-entropy carbide consolidated via spark plasma sintering of TaC, ZrC and NbC. *Scr. Mater.* **164**, 12–16 (2019).

24. Han, X. *et al.* Improved creep resistance of high entropy transition metal carbides. *J. Eur. Ceram. Soc.* **40**, 2709–2715 (2020).

25. Fahrenholtz, W. G. & Hilmas, G. E. Ultra-high temperature ceramics : Materials for extreme environments. *Scr. Mater.* **129**, 94–99 (2017).

26. Mayrhofer, P. H., Kirnbauer, A., Ertelthaler, P. & Koller, C. M. High-entropy ceramic thin films; A case study on transition metal diborides. *Scr. Mater.* **149**, 93–97 (2018).

27. Kirnbauer, A. *et al.* Thermal stability and mechanical properties of sputtered (Hf ,Ta ,V ,W ,Zr)-diborides. *Acta Mater.* **200**, 559–569 (2020).

28. Kang, W., Merrill, M. & Wheeler, J. M. In situ thermomechanical testing methods for micro/nano-scale materials. *Nanoscale* **9**, 2666–2688 (2017).

29. Wheeler, J. M. & Michler, J. Invited article: Indenter materials for high temperature nanoindentation. *Rev. Sci. Instrum.* **84**, 1–11 (2013).

30. Yu, X. *et al.* Constitutive law and flow mechanism in diamond deformation. *Sci. Rep.* **2**, 1–7 (2012).

31. Mayrhofer, P. H., Kunc, F., Musil, J. & Mitterer, C. A comparative study on reactive and non- reactive unbalanced magnetron sputter deposition of TiN coatings. *Thin Solid Films* **415**, 151–159 (2002).